Far-Field Spectroscopy and Near-Field Optical Imaging of Coupled Plasmon–Phonon Polaritons in 2D van der Waals Heterostructures

Xiaoxia Yang, Feng Zhai, Hai Hu, Debo Hu, Ruina Liu, Shunping Zhang, Mengtao Sun, Zhipei Sun, Jianing Chen,* and Qing Dai**

Plasmonic nanostructures can concentrate and manipulate electromagnetic fields at the subwavelength scale, enabling numerous, fast, compact, and efficient optical devices, such as light sources, waveguides, and detectors with high spatial and temporal resolution, metamaterials, quantum optics, photovoltaic devices, and sensors.[1,2] However, applications based on conventional plasmonic nanostructures seriously suffer from large Ohmic losses in noble metals and relatively short (typically ≈10 fs)[3,4] lifetime of the localized plasmons.[5,6] Long-range surface plasmon polaritons have been demonstrated with relatively long lifetime, but typically scarifying plasmon confinement performance.[7,8] Recently, graphene has been demonstrated as a promising plasmonic material for manipulating electromagnetic signals at the deep-subwavelength scale with ultrahigh speed and very low energy consumption owing to the unique properties of Dirac Fermions in graphene.[9–13] Intrinsic graphene plasmons are predicted to have a long lifetime reaching hundreds of optical cycles,[4,14] which is of great interest for various applications such as single-photon nonlinearity[15–17] and deep subwavelength metamaterials.[18–20] However, strong plasmon damping has been experimentally observed mainly due to large scattering from substrate surface phonons and impurity charges, leading to very short graphene plasmon lifetime. For example, the lifetime of graphene plasmons on a SiO_2/Si substrate is smaller than 100 fs (corresponding to approximately two plasmon wavelengths of propagation distance),[12,21] far below the theoretically predicted value.[4,14] Substrates (e.g., hexagonal boron nitride (*h*-BN)) that can mostly maintain the superior properties of graphene plasmons have been demonstrated to support high mobility graphene[22] with relatively long lifetime (e.g., ≈500 fs, corresponding to ≈9 plasmon wavelengths),[23] and thus have attracted great research interest in the field of graphene plasmonics.[23–26] Furthermore, the 2D *h*-BN van der Waals material, as a kind of hyperbolic material, can enable sub-diffraction-limited, highly directional, and spatially confined hybrid polariton modes,[27–30] preserving the characteristics of plasmon and phonons.

Here we observe a new hybridized plasmon–phonon polariton (PPP) mode in graphene/*h*-BN van der Waals heterostructures due to the interaction between graphene plasmon and the out-of-plane transverse optical (*o*-TO) phonon in monolayer *h*-BN. Such PPP mode does not exist in conventional bulk materials (e.g., SiO_2), because the effective electric potential of TO phonons is zero and therefore surface optical (SO) phonons dominate the plasmon–phonon interaction at the interface of the bulk substrate and graphene.[31,32] Our observation of this new PPP mode is explained by the interaction between highly localized graphene plasmon electromagnetic field and the resonant polarization of the monolayer *h*-BN lattice. Furthermore, in contrast to the previous efforts that consider phonon interaction as a major damping effect of graphene plasmons,[14] we demonstrate that such plasmon–phonon interaction can significantly facilitate the generation of hybrid graphene plasmons with ultralong lifetime (calculated from the linewidths of the resonance peaks). In this concept (**Figure 1**a), the lifetime of the hybrid graphene plasmons is determined by the contributions from both plasmon-like and phonon-like characters. In our experiment, monolayer *h*-BN is selected to support weakly damped phonon polaritons in the midinfrared range due to weak phonon–phonon scattering.[33–35] Therefore, extremely long hybrid plasmon lifetime (calculated up to 1.6 ps) on the picosecond scale has been successfully achieved near the energy of the *h*-BN optical phonon at 820 cm^{-1} with the hybrid PPP mode method. Our results show that it is an effective approach to tune the plasmon behavior in the frequency, time and space domains.

In order to achieve strong plasmon–phonon hybridization in graphene/*h*-BN heterostructure, we designed and fabricated various graphene nanoribbon arrays on monolayer *h*-BN (Figure 1b). Graphene is first transferred on top of monolayer

X. Yang, H. Hu, D. Hu, R. Liu, Prof. Q. Dai
National Center for Nanoscience and Technology
Beijing 100190, China
E-mail: daiq@nanoctr.cn
Prof. F. Zhai
Department of Physics
Zhejiang Normal University
Jinhua 321004, China
Prof. S. Zhang
Department of Physics
Wuhan University
Wuhan 430072, China
Prof. M. Sun, Prof. J. Chen
Institute of Physics
Chinese Academy of Science, and Collaborative Innovation Center of Quantum Matter
Beijing 100190, China
E-mail: jnchen@iphy.ac.cn
Prof. Z. Sun
Department of Micro- and Nanosciences
Aalto University
Tietotie 3, FI-02150 Espoo, Finland
E-mail: zhipei.sun@aalto.fi

DOI: 10.1002/adma.201505765

 © 2016 WILEY-VCH Verlag GmbH & Co. KGaA, Weinheim

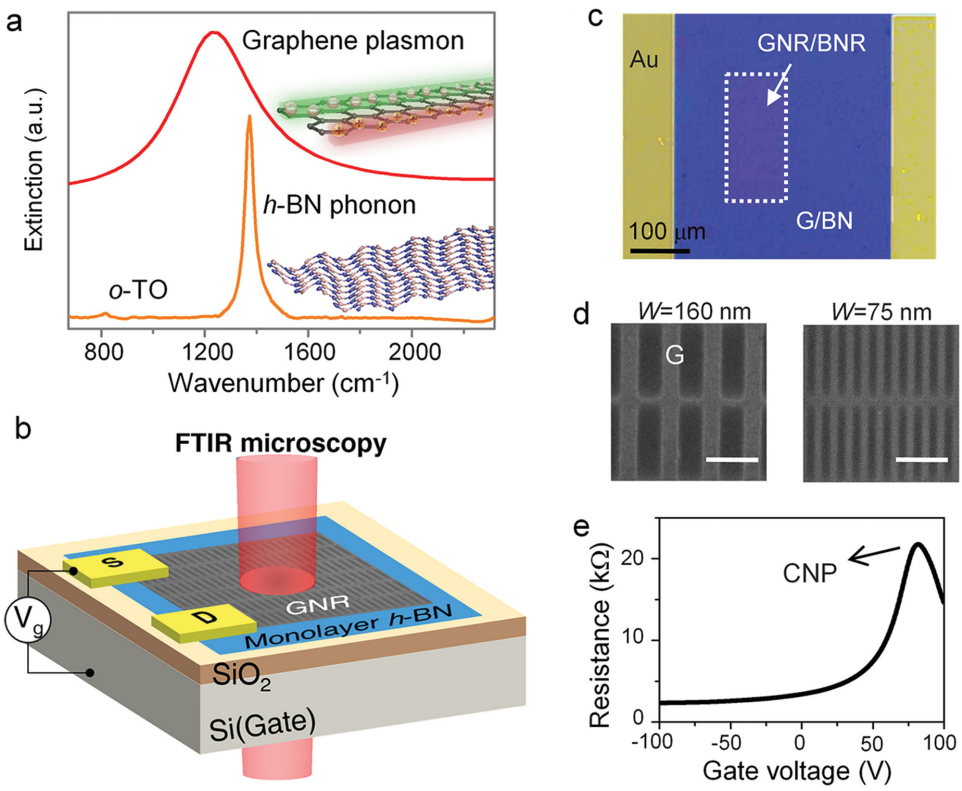

Figure 1. Concept, measurement setup, and device. a) Graphene plasmon and *h*-BN phonon polariton can strongly couple in the mid-infrared range. This forms new hybridization plasmon–phonon polariton modes, combining unique properties of plasmon and phonon (e.g., strong field enhancement of plasmon and long lifetime of phonon polariton). b) FTIR measurement scheme for electrically tunable GNR/BNR heterostructures. The monolayer *h*-BN under GNR is also etched into nanoribbons. The mid-IR spot size is about 100×100 μm^2. c) Optical image of the device. d) SEM images of graphene nanoribbon arrays (light gray) with different ribbon widths. Scale bars are 500 nm. e) Gate-dependent resistance of the graphene/*h*-BN heterostructure ($W = 160$ nm).

h-BN, which is placed on a SiO_2/Si substrate (details in the Experimental Section). Then graphene and *h*-BN are patterned together into electrically continuous nanoribbon arrays with a 1:2 width-to-pitch ratio. Ti/Au electrodes (Figure 1c) are deposited to electrically tune the doping level of graphene nanoribbons with the heavily doped Si layer as the back-gate electrode. Different devices with ribbon width W ranging from 55 to 220 nm are fabricated to understand plasmon–phonon interaction as a function of wave vector q ($q = \pi/W$). Devices with $W = 75$ and 160 nm are shown in Figure 1d. Gate voltage (V_g) dependent resistance curve of the graphene/*h*-BN heterostructures is used to calculate the graphene Fermi level (E_F) and determine the charge neutral point (CNP, i.e., $E_F = 0$ eV). Our 160 nm wide graphene nanoribbon device (Figure 1e) gives the CNP at the V_g of 82 V, indicating that the graphene layer was hole-doped at zero gate voltage. Similar CNP value is observed for different W devices. We also fabricated various graphene nanoribbon arrays with different ribbon widths directly on SiO_2/Si substrates for comparison.

After fabrication, we studied the plasmon–phonon interaction by a Fourier transform infrared (FTIR) spectroscopy (Figure 1b). This method is unique to investigate plasmon–phonon coupling, and has been well-known as an effective method to determine plasmon lifetime in various graphene devices,[18–21,24,34,36,37] as such microscopic approach can disentangle different plasmon damping mechanisms in samples with large detection area (up to 10 mm × 10 mm), broad infrared spectral range (≈400–4000 cm^{-1}), and high collective excitation efficiency.[38] **Figure 2**a shows the extinction spectra of three different samples, i.e., monolayer graphene/*h*-BN nanoribbon/SiO_2 (G/BNR), monolayer graphene nanoribbon/*h*-BN nanoribbon/SiO_2 (GNR/BNR), and monolayer graphene nanoribbon/SiO_2 (GNR/SiO_2). $W = 100$ nm is chosen for all three devices. The extinction spectra are given by the normalized transmittance spectra T (when $E_F = 0.35$ eV) relative to the transmittance at the CNP (T_{CNP}) as $1-T(E_F = -0.35\ \text{eV})/T_{CNP}$. The extinction spectrum of the G/BNR device is flat, showing that individual *h*-BN nanoribbons contribute to no resonance peak in the measured extinction spectrum range (either from BNR phonon polaritons or from graphene plasmons excited by the BNR substrate). Identical results were also observed with all G/BNR devices with different E_F and ribbon width W, further confirming that the contribution of individual *h*-BN nanoribbons to the extinction spectrum can be neglected in our experiments.

As shown in Figure 2a, the extinction spectrum (purple solid line) of the GNR/SiO_2 device typically has three peaks (purple triangles), named as Peak α (at ≈786 cm^{-1}) , Peak β (at ≈900 cm^{-1}), Peak γ (at ≈1332 cm^{-1}). They are assigned to graphene plasmons interacted with two surface optical phonons:

© 2016 WILEY-VCH Verlag GmbH & Co. KGaA, Weinheim

15214095, 2016, 15, Downloaded from https://advanced.onlinelibrary.wiley.com/doi/10.1002/adma.201505765 by National Center For, Wiley Online Library on [15/10/2025]. See the Terms and Conditions (https://onlinelibrary.wiley.com/terms-and-conditions) on Wiley Online Library for rules of use; OA articles are governed by the applicable Creative Commons License

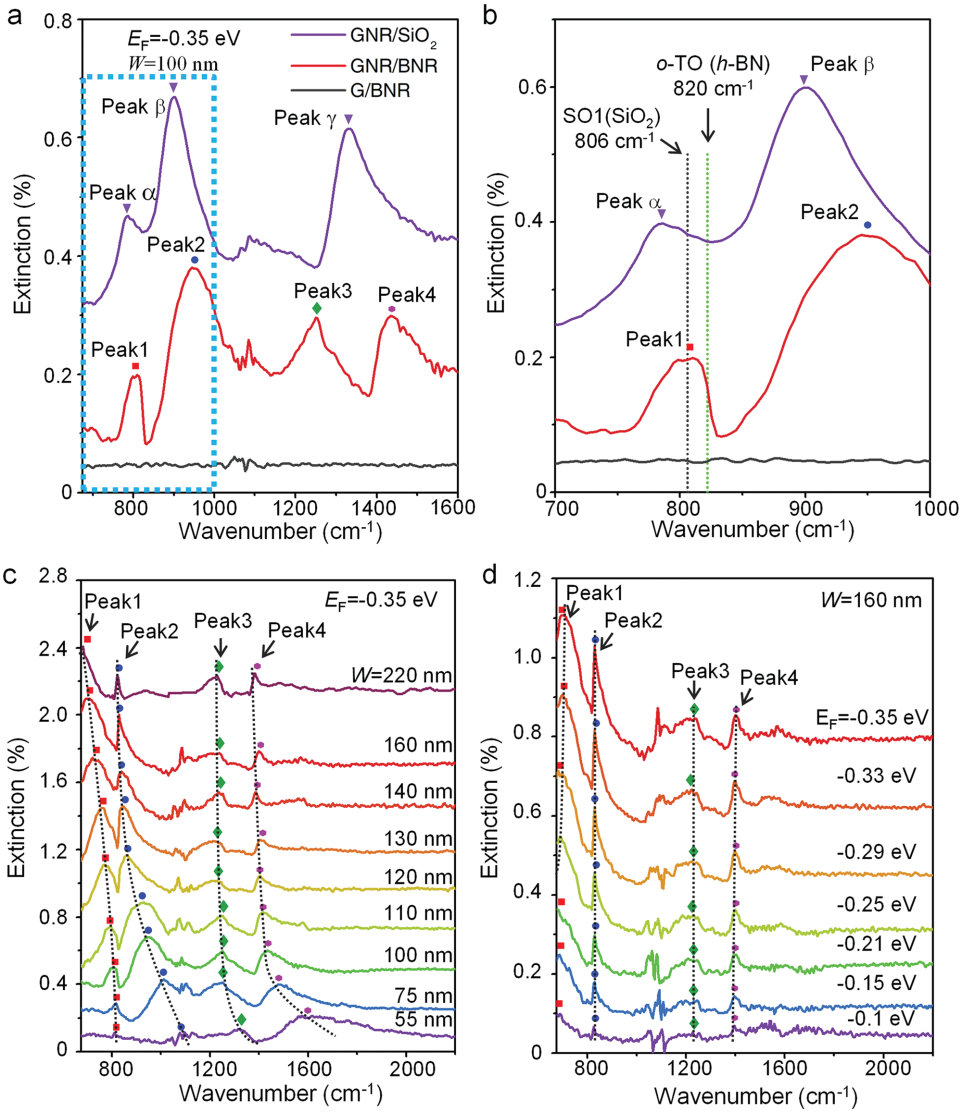

Figure 2. Plasmonic response of graphene/*h*-BN heterostructures. a) Extinction spectra of our G/BNR, GNR/BNR, and GNR/SiO_2 devices. The ribbon width is 100 nm with $E_F = -0.35$ eV. b) Enlarged view of the first two peaks at low-energy spectral range displayed in (a). The dotted vertical lines indicate the SO phonon of SiO_2 at 806 cm^{-1} and the *h*-BN phonon at 820 cm^{-1}. c) Extinction spectra of the GNR/BNR devices with varying ribbon widths. $E_F = -0.35$ eV. d) Extinction spectra of the GNR/BNR device at varied E_F. The ribbon width is 160 nm. The colored dots and dotted lines indicate the change of the resonance peaks.

phonons at ≈806 cm^{-1} (named as SO1 phonon) and ≈1168 cm^{-1} (named as SO2 phonon) of the SiO_2 substrate.[21] In our GNR/BNR device (red solid line), we normally observe peaks at 809 cm^{-1} (Peak 1, square dot), 950 cm^{-1} (Peak 2, round dot), and 1251 cm^{-1} (Peak 3, diamond dot), similar to the GNR/SiO_2 device. However, a close observation (Figure 2b) presents significantly new features in our GNR/BNR device, except for Peak 3, which has been assigned to the SO2 phonon of the SiO_2 substrate.[23] The anticrossing energy center between Peak 1 (square dots) and Peak 2 (round dots) shifts to ≈820 cm^{-1} (green dotted line in Figure 2b) in the GNR/BNR device, with no energy loss at ≈806 cm^{-1} (black dotted line in Figure 2b, the anticrossing energy center observed in the GNR/SiO_2 device, associated with the SO1 phonon of the SiO_2 substrate). This denotes that monolayer *h*-BN ribbon can effectively isolate the influence of the SO1 phonon from the beneath SiO_2 substrate in our GNR/BNR heterostructure. We assign the new anticrossing behavior at 820 cm^{-1} as a new PPP mode, due to the coupling between graphene plasmons and the out-of-plane transverse optical (*o*-TO) phonon (typically at ≈820 cm^{-1})[39] of the monolayer *h*-BN substrate. Worth noting that it is the first time that such coupling between transverse optical (i.e., *o*-TO) phonon and surface plasmon is observed. A new resonant peak at >1370 cm^{-1} (Peak 4, hexagon dot in Figure 2a) is also observed, which has been assigned in previous study as the longitudinal optical (LO) phonon of *h*-BN.[24] Our results show that highly confined graphene plasmons enable strong interaction with their atomically thin local dielectric environment (i.e., the LO and *o*-TO phonons of *h*-BN), and generate distinguishing hybridized PPP modes in the heterostructures.

© 2016 WILEY-VCH Verlag GmbH & Co. KGaA, Weinheim

15214095, 2016, 15, Downloaded from https://advanced.onlinelibrary.wiley.com/doi/10.1002/adma.201505765 by National Center For, Wiley Online Library on [15/10/2025]. See the Terms and Conditions (https://onlinelibrary.wiley.com/terms-and-conditions) on Wiley Online Library for rules of use; OA articles are governed by the applicable Creative Commons License

To further understand the hybridized PPP modes, we measured the extinction spectra of our GNR/BNR devices with different graphene ribbon widths W (Figure 2c) and at different Fermi energy levels E_F (Figure 2d). All spectra are normalized relative to the spectra measured at the CNP (i.e., $E_F = 0$). We observe that the energy distribution of all hybridized plasmon resonance modes redshifts when W increases (or when $|E_F|$ decreases). This matches well with the shift of the graphene intrinsic plasmon (ω_{pl}), determined by E_F and W via $\omega_{p1} = \sqrt{e^2 E_F q / (2\pi\hbar^2 \varepsilon_0 \varepsilon_r)}$, where $q = \pi/W$.[40,41] For example, Peak 1 shifts from 817 to 675 cm^{-1}, when W increases from 55 to 220 nm. This further verifies that the h-BN monolayer can effectively isolate the influence of the SO1 phonon from the beneath SiO_2 substrate in our GNR/BNR heterostructures, as the anticrossing behavior introduced by the SO1 phonon in the SiO_2 substrate typically appears at ≈806 cm^{-1} with the Peak α located at less than ≈806 cm^{-1} (Figure S4 and S5, Supporting Information). We also notice that the linewidths of all hybridized PPP modes change with E_F and W. This suggests that both the spatial and temporal performance of all hybridized PPP modes can be controlled by the electrical gating and physical dimension (e.g., the width) of graphene ribbons.

The electromagnetic coupling of the graphene plasmons with the LO phonon in van der Waals heterostructures has been investigated previously,[24,42] however, the interaction between the graphene plasmon and the TO phonon, observed here, has been long considered unachievable. It is because the effective electric potential of the TO phonons in conventional bulk materials (e.g., SiO_2) is zero and thus the TO phonons have no interaction with the plasmons.[31,32] In contrast to the convention bulk materials, this interaction is possible in our GNR/BNR heterostructure, and can be explained by a classic electromagnetic coupling theory: the strongly confined near-field electric field $\boldsymbol{E}$ of the graphene plasmon (white arrows in **Figure 3**a) introduces displacement of h-BN lattices (Figure 3a).

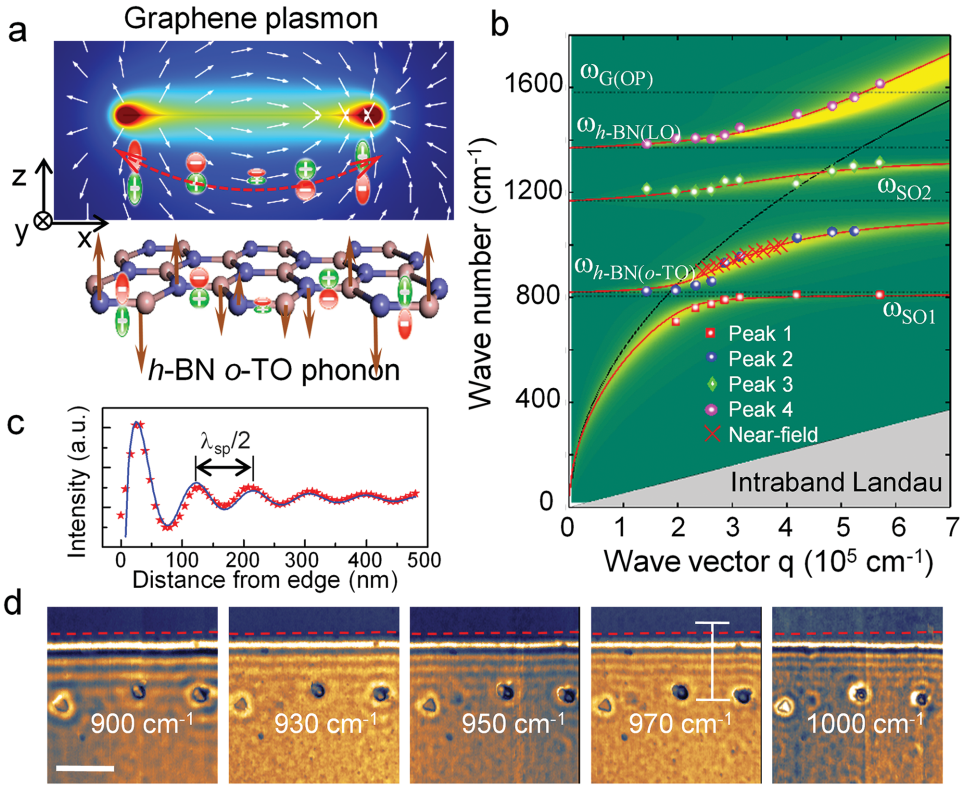

Figure 3. The coupling mechanism of graphene plasmons and the h-BN optical phonons. a) Theoretically calculated electric-field intensity $|\boldsymbol{E}|^2$ distribution and electric field directions (white arrows) of graphene plasmons on the cross-section of the graphene/h-BN heterostructure (W = 100 nm and E_F = –0.35 eV at the extinction maximum at the plasmon resonance frequency). The h-BN o-TO phonon hybridizes with graphene plasmon through the interaction between the electric dipoles and electric field of graphene plasmon in the z direction. The induced o-TO phonon polariton is marked as red arrow. b) Plasmon frequencies as a function of wave vector for different hybridized mode peaks. The calculated dispersion relation is plotted as red lines and the loss function is plotted as a 2D pseudo-color background. The dashed line refers to graphene plasmon dispersion without phonon hybridization. The experimental results are also given (square dots, round dots, diamond dots, and hexagon dots for Peaks 1, 2, 3, and 4, respectively). The red crosses show the experimental results extracted from the near-field measurements in (c) and (d). The frequencies of the SO phonons of SiO_2 and the o-TO and LO phonons of h-BN are marked as horizontal dotted lines. The gray area is the intraband Landau damping area. c). Line profile of s-SNOM optical signals at the excitation wavelength of 970 cm^{-1}. The results are fitted with the method described by Woessner et al.[23] The distance between two peaks corresponds to half of the plasmon wavelength λ_p. d) s-SNOM images from 2D scan of the tip position near the graphene edge (dashed line) with varied excitation wavelengths. The location of the graphene edge was determined from the simultaneously measured topography. Scale bar is 500 nm.

© 2016 WILEY-VCH Verlag GmbH & Co. KGaA, Weinheim

15214095, 2016, 15, Downloaded from https://advanced.onlinelibrary.wiley.com/doi/10.1002/adma.201505765 by National Center For, Wiley Online Library on [15/10/2025]. See the Terms and Conditions (https://onlinelibrary.wiley.com/terms-and-conditions) on Wiley Online Library for rules of use; OA articles are governed by the applicable Creative Commons License

The lattice displacement strongly depends on the direction and intensity of $\boldsymbol{E}$. It is particularly large when the lattices are close to the edges of graphene ribbons, where the effective near-field of graphene plasmons has a maximum component in the z direction (the case corresponding to the maximum oscillation amplitude of graphene plasmon is shown in Figure 3a). Neglecting the retardation effect, the lattice displacement periodically responds to the graphene plasmon resonance, forming phonon polariton resonance (red arrow in Figure 3a) with identical wave vector and wavelength to the graphene plasmon. As a result, the hybridization between the graphene plasmon and the *o*-TO phonon occurs. As absent in bulk substrates, this coupling of the *o*-TO phonon with graphene plasmon is a unique PPP mode, which unusually exists in monolayer van der Waals crystal (such as *h*-BN) heterostructures.

In our experiments, monolayer *h*-BN is particularly used in our heterostructure, which has only three optical phonons due to its simple atomic structure: LO, *o*-TO and in-plane (*i*-TO) phonons. Consequently, the local polarization electric potentials (Φ) of the optical phonons can be well calculated to understand the abovementioned new coupling physics using a remote phonon scattering mechanism.[31] In the long wavelength limit, the Φ_λ generated from the polarization field of optical phonon λ at a position of $\boldsymbol{r} = x\mathbf{e}_{\perp} + y\mathbf{e}_{i_T} + z\mathbf{e}_{o_T}$ $(z > 0)$ is calculated as:

$$\Phi_\lambda(\boldsymbol{r}) = \sum_l \frac{e n_B^\lambda u_{\lambda \mathrm{q}} \mathbf{e}_\lambda \cdot \mathbf{r}_l}{4\pi\varepsilon_0 r_l^3} \exp(i\mathbf{q}\cdot\mathbf{R}_l),\ \mathbf{r}_l = \mathbf{r} - \mathbf{R}_l \quad (1)$$

where $\boldsymbol{e}_L$, $\boldsymbol{e}_{\mathrm{lt}}$, and $\boldsymbol{e}_{\mathrm{oT}}$ is the atom vibration directions of LO (along x), *i*-TO (along y) and *o*-TO (along z), and $e n_B^\lambda u_{\lambda q} e_\lambda \exp(i\mathbf{q}\cdot\mathbf{R}_l)$ is the dynamic dipole momentum introduced by relative lattice displacement. Then the summation of $\Phi_\lambda(\boldsymbol{r})$ over a lattice vector $\boldsymbol{R}_l$ gives the effective Φ_λ. Details of the calculation are fully described in the Supporting Information. The calculations give nonzero Φ for LO and *o*-TO phonons (i.e., $\Phi_{\mathrm{L}} \neq 0$, $\Phi_{\mathrm{oT}} \neq 0$), further validating the interaction between the graphene plasmons and the *o*-TO (and LO) phonons. Based on the values of obtained Φ, the Fröhlich-like coupling strength $F_{i,\lambda}^2$ (i and λ represent the substrate and the phonon type, respectively) between plasmons and different phonon modes is calculated with a generalized random phase approximation theory (RPA).[21,43] The simulation results (details in the Supporting Information) are shown in Figure 3b, fitting extremely well with our experimental results (dots in Figure 3b). In our simulation, $F_{\mathrm{SiO_2,SO1}}^2 = 0$, $F_{\mathrm{SiO_2,SO2}}^2 = 0.44$ meV, $F_{h-\mathrm{BN},o-\mathrm{TO}}^2 = 0.08$ meV and $F_{h-\mathrm{BN,LO}}^2 = 0.42$ meV are used. The nonzero coupling strengths ($F_{h-\mathrm{BN},o-\mathrm{TO}}^2$ and $F_{h-\mathrm{BN,LO}}^2$) for the *h*-BN *o*-TO and LO phonons support that both phonon modes are hybridized with graphene plasmons (as observed in our experiments), but the zero coupling strength $F_{\mathrm{SiO_2,SO1}}^2$ suggests that there is no coupling between the SiO_2 SO1 phonon and graphene plasmon in our GNR/BNR heterostructure. This is because graphene plasmon polarization and effective potential of the *o*-TO phonon in *h*-BN destructively interfere each other, generating weak hybridization with the SO1 phonon of the SiO_2 when they are in resonance.[24]

In order to directly observe propagation of the hybridized PPP modes, we performed near-field optical characterization of a graphene/*h*-BN heterostructure using a scattering-type scanning near-field optical microscopy (s-SNOM) with variable excitation frequency from 900 to 1000 cm^{-1} (details in the Experimental Section). Figure 3c,d plots line profile and images of s-SNOM optical signals at the graphene edges. This clearly shows the hybridized PPP modes can propagate along the graphene surface and reflect at the graphene edge. The plasmon wavelength λ_p and the corresponding wave vector q_p can be calculated from the spatial variation of these images, as shown in Figure 3b (magenta crosses). These near-field propagation results coincide exactly with the far-field data (blue dots) and the theoretical prediction (lines), validating the far-field results obtained with the FTIR method.

As discussed, the *o*-TO phonon and graphene plasmon hybridization is a novel coupling mode exceptionally appearing in the heterostructures of graphene and van der Waals crystals (in contrast to other bulk substrates (e.g., SiO_2) based graphene devices). This new coupling mode can offer extraordinary opportunities to manipulate the graphene plasmon behavior. For example, here we demonstrate to increase the lifetime of graphene plasmons with such hybridization, because the *o*-TO phonon lifetime in monolayer *h*-BN is significantly long. In fact, this has already been presented when comparing the linewidth change of the peaks (near the anticrossing energy) between GNR/SiO_2 and GNR/BNR devices (Figure 2b). To fully investigate this application of using the newly-observed PPP mode to lengthen plasmonic lifetime quantitatively, we extract the lifetimes and peak positions of the resonance peaks (E_{res}). For the far-field extinction spectra of graphene devices, the linewidth Γ of resonance peaks is connected to the damping rate, and thus can be used to calculate the lifetime T by an equation of $T = 2/\Gamma$.[3,44] With this equation, the lifetime of all hybridized modes is calculated with Γ, which is extracted by Fano curve fitting (see **Figure 4**a and calculation methods in the Supporting Information).[20,45] The lifetime of the PPP mode at ≈820 cm^{-1}, extracted from the extinction spectra around Peak 2 in Figure 2c,d, is plotted as a function of E_F (upper panel in Figure 4b) and W (lower panel in Figure 4b). As shown in Figure 4b, when the PPP mode location is adjusted (by E_F or W) closer to the *h*-BN *o*-TO phonon at 820 cm^{-1}, its lifetime become longer because the phonon-like character mainly defines the hybrid PPP mode behavior (including the lifetime).[21,46] However, as the PPP mode is close to the phonon frequency, its intensity decreases. Therefore, the low intensity of Peak 2 (e.g., when $|E_F| < 0.1$ eV, the signal is <0.005% which is too small to be measured in our experiment) limits a longer lifetime measurement, anticipated for smaller $|E_F|$ and larger W. The maximum observed lifetime of the PPP mode near the energy of the *h*-BN *o*-TO phonon at ≈820 cm^{-1} is ≈1.6 ± 0.1 ps. Worth noting that the size of such hybrid long-lifetime modes can be >80 times smaller than the incident wavelength, featuring strong spatial confinement (up to $\approx\lambda_0^2/7000$) property of graphene plasmons (in contrast to the small confinement of long-range plasmons). The origin of such remarkably long hybrid plasmon lifetime on the picosecond scale in our GNR/BNR heterostructure is because the *o*-TO phonon contributed to the mode hybridization has a long lifetime. Worth noting that currently our measured result is about three times longer than the best plasmon lifetime in previously reported graphene/*h*-BN devices,[23] but in principle much longer hybrid plasmon lifetime can

© 2016 WILEY-VCH Verlag GmbH & Co. KGaA, Weinheim

15214095, 2016, 15, Downloaded from https://advanced.onlinelibrary.wiley.com/doi/10.1002/adma.201505765 by National Center For, Wiley Online Library on [15/10/2025]. See the Terms and Conditions (https://onlinelibrary.wiley.com/terms-and-conditions) on Wiley Online Library for rules of use; OA articles are governed by the applicable Creative Commons License

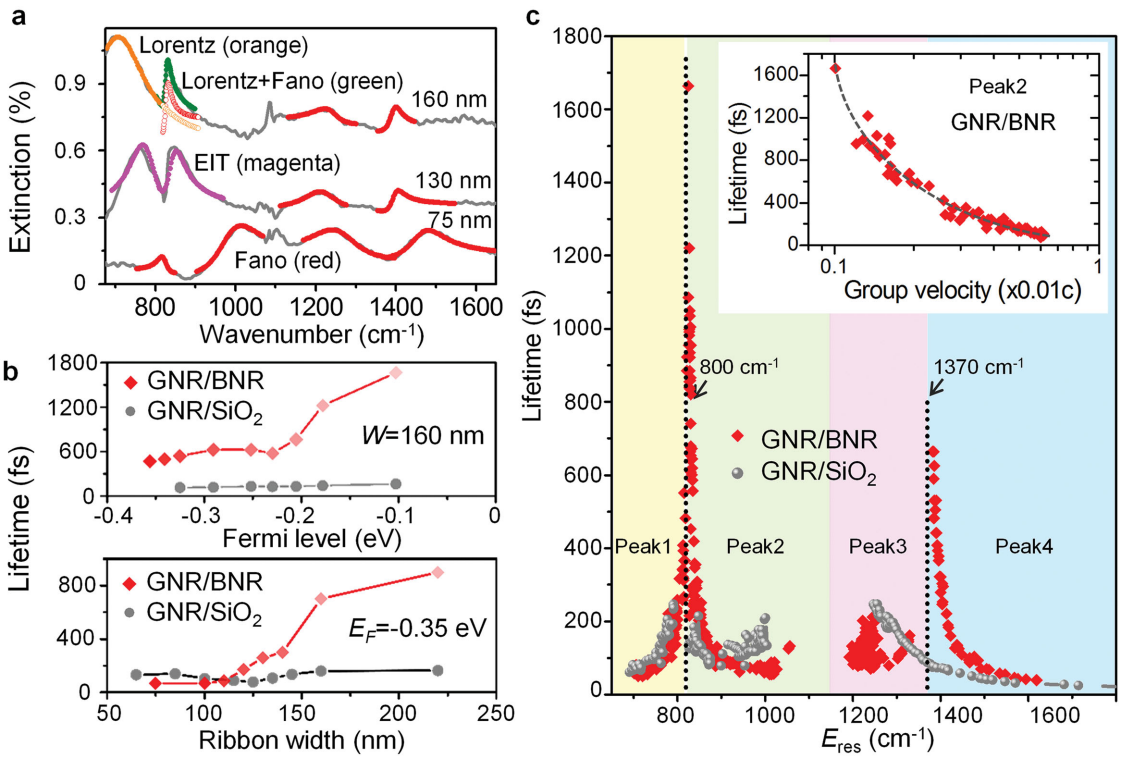

Figure 4. Hybridized plasmon lifetime of our GNR/BNR devices. a) Illustration of the curve analysis methods to extract the full width at half-maximum (FWHM) (Γ) of resonance peaks. Fano model is used to fit the coupled peaks (red curves). Electromagnetic induced transparent (EIT) model is adapted when pristine plasmon frequency is close to the phonon frequency of substrate (purple curves). The plasmonic peak is fitted by Lorentz shape (orange curves) whose tail is taken as the continuum background for Fano fitting. The superposition of the Fano fitted line shape and the background reconstructs the green peak. b) Hybridized plasmon lifetime of GNR/BNR (red) and GNR/SiO_2 (gray) devices (extracted from Peak 2 and Peak β in Figure 2c,d) as a function of E_F and W, respectively. c) The hybridized plasmon lifetimes of all peaks taken from GNR/BNR (red) and GNR/SiO_2 (gray) devices with different W and at different E_F are plotted together as a function of plasmon resonance frequency. The dotted lines indicate the o-TO phonon (at 820 cm^{-1}) and LO phonon (at 1370 cm^{-1}) of h-BN monolayer. Inset: The relationship between the lifetime and the group velocity of hybrid PPP modes.

be anticipated with this concept. For example, longer hybrid plasmon lifetime, comparable to the long intrinsic lifetime of phonon, is achievable, by using monolayer h-BN (Figure S7, Supporting Information) or high-quality mechanically exfoliated h-BN or improving the coupling efficiency in heterostructure devices (e.g., using 2D materials with phonons having larger dynamic dipole moment).

The lifetimes of other three hybrid modes from our GNR/BNR devices with different W and E_F are plotted in Figure 4c. We observe similar lifetime tendency on these modes: lifetime increases dramatically when their resonance frequency E_{res} approaches to the corresponding optical phonon frequencies of h-BN at 820 (the o-TO phonon) and 1370 cm^{-1} (the LO phonon). The maximum lifetime (663 fs) of the PPP mode hybridized with the LO phonon is around one-third of the maximum lifetime of the PPP mode hybridized with the o-TO phonon. This is due to that the LO phonon of h-BN typically has much shorter lifetime than the o-TO phonon, because LO phonon can be easily scattered into i-TO phonon due to the energy matching.[47] We also find that the hybrid graphene plasmon lifetime decreases sharply as E_{res} is close to or larger than the origin optical phonon of graphene at 1580 cm^{-1} (e.g., the 55 nm wide ribbon device in Figure 2c). This is attributed to the decay of graphene plasmon into electron–hole pairs via the optical phonon emission in graphene,[21] as expected and shown in Figure 3b. As a contrast, the lifetime of our reference GNR/SiO_2 devices is also plotted in Figure 4c. The lifetime increases slowly around the SO phonon frequencies of SiO_2 at 806 and 1168 cm^{-1}. The maximum hybrid graphene plasmon lifetime in the reference GNR/SiO_2 devices is about 240 fs, which is around seven times shorter than that of our GNR/BNR device. This underscores the advantage of using the o-TO phonon of h-BN to increase the graphene plasmon lifetime while maintaining high mode confinement.

The coupling with the h-BN optical phonons also affects the group velocity v_g of plasmons significantly, which is determined by $\partial\omega/\partial q$. As seen from Figure 3b, for all modes, v_g decreases drastically when the mode frequency is approaching the phonon energy. We plot the measured lifetime and the estimated group velocity of the hybrid PPP modes (for Peak 2) in the inset of Figure 4c. It shows that the hybrid PPP modes possess an ultrasmall group velocity down to 0.001c, where c is the speed of light in vacuum. The combination of small group velocity and the field enhancement associated with plasmon characteristic of the hybrid PPP modes presents new opportunities for various photonic applications, e.g., enhanced

© 2016 WILEY-VCH Verlag GmbH & Co. KGaA, Weinheim

15214095, 2016, 15, Downloaded from https://advanced.onlinelibrary.wiley.com/doi/10.1002/adma.201505765 by National Center For, Wiley Online Library on [15/10/2025]. See the Terms and Conditions (https://onlinelibrary.wiley.com/terms-and-conditions) on Wiley Online Library for rules of use; OA articles are governed by the applicable Creative Commons License

nonlinear light-matter interaction for high-efficiency frequency conversion in the IR and THz spectral range.

In conclusion, we demonstrate that the interaction between plasmons and phonons can significantly increase the calculated hybrid plasmon lifetime up to ≈1.6 ps. Such extraordinarily long lifetime arises from the counterintuitive coupling of the long-lifetime out-of-plane transverse optical phonon in *h*-BN. Our demonstration and in-depth understanding of the new plasmon–phonon polariton mode not only reveal a new plasmon–phonon coupling mechanism in van der Waals heterostructures, but also offer a novel approach to tune the plasmon behavior in the frequency, time, and space domains, introducing a new paradigm to enable novel plasmon–phonon polariton devices (such as deep-wavelength metamaterials,[48] ultralow-loss waveguides),[49,50] where ultralong-lifetime and low-damping polaritons are needed.

Experimental Section

Fabrication of Monolayer Graphene/h-BN Heterostructures: Graphene and monolayer *h*-BN sheets were both grown on copper foil via chemical vapor deposition (CVD) and then transferred to target substrates using a standard wet method.[51] First, *h*-BN monolayer was transferred onto SiO_2/Si substrate, and then graphene sheet was transferred onto the *h*-BN. Next, nanoribbon arrays were patterned in the graphene and *h*-BN using 100 keV electron-beam lithography (EBL) (Vistec 5000+ES, Germany) on approximately 260 nm of poly(methyl methacrylate) (PMMA, MicroChem), followed by oxygen plasma etching at 5 Pa and 100 W for 8 s. Two Ti (2 nm)/Au (40 nm) electrode patterns were defined using a second EBL process and electron beam evaporation.

Characterization of Graphene/h-BN Heterostructures: Dimensions of the patterned graphene nanoribbons were characterized by using scanning electron microscopy (SEM, Hitachi S-4800) and atomic force microscopy (AFM, Bruker Dimension Icon) (refer to the Supporting Information). Graphene quality was confirmed by Raman spectroscopy (Horiba Jobin Yvon LabRAM HR800) before and after oxygen ion bombardment under the protection of PMMA. The electrical transport properties were characterized using a semiconductor parameter analyzer (Keithley 4200-SCS) at room temperature.

Fourier Transform Infrared Microscopy Measurements: Infrared transmission measurements were performed using a FTIR microscopy (Thermo Fisher Nicolet iN10). Single-beam transmittance spectra at the charge neutral point were used as a background to calculate the extinction spectra of the doped graphene nanoribbons. Each measurement was obtained with its own background spectrum and was repeated several times to confirm the extinction spectrum. All measurements were performed at room temperature and in an atmospheric environment.

Near-Field Optical Microscopy Measurements: Near-field results were measured using a scattering SNOM (Neaspec GmbH), equipped with wavelength-tunable lasers (between 900 and 1000 cm^{-1}). The probes were commercially available metallized AFM probes with an apex radius of ≈25 nm (Nanoworld). Due to multiple reflection of plasmon waves at the edges of the nanoribbons, it is challenging to measure near-field signals in our nanoribbon graphene devices. Therefore, a mechanically exfoliated graphene/BN sample is used to characterize propagation property of PPP modes. The optical signals were obtained from the fourth harmonic interferometric pseudo-heterodyne signal.

Supporting Information

Supporting Information is available from the Wiley Online Library or from the author.

Acknowledgements

The authors thank P. Alonso-Gonzalez, A. Y. Nikitin for near-field characterizing and simulating discussions. This work was supported by the National Basic Key Research Program of China (Grant Nos. 2015CB932402 and 2014CB921001), the National Natural Science Foundation of China (Grant Nos. 51372045, 11474350, and 11174252), and Academy of Finland (Grant Nos. 276376, 284548, and 285972), and "Strategic Priority Research Program (B)" of the Chinese Academy of Sciences (Grant No. XDB07030200), and the European Union's Seventh Framework Programme (REA Grant Agreement No. 631610).

Received: November 21, 2015
Revised: December 29, 2015
Published online: February 18, 2016

[1] E. Ozbay, *Science* **2006**, *311*, 189.
[2] D. K. Gramotnev, S. I. Bozhevolnyi, *Nat. Photonics* **2010**, *4*, 83.
[3] C. Sönnichsen, T. Franzl, T. Wilk, G. von Plessen, J. Feldmann, *Phys. Rev. Lett.* **2002**, *88*, 077402.
[4] M. Jablan, H. Buljan, M. Soljacic, *Phys. Rev. B* **2009**, *80*, 245435.
[5] J. B. Khurgin, *Nat. Nanotechnol.* **2015**, *10*, 2.
[6] A. Boltasseva, H. A. Atwater, *Science* **2011**, *331*, 290.
[7] R. F. Oulton, V. J. Sorger, D. A. Genov, D. F. P. Pile, X. Zhang, *Nat. Photonics* **2008**, *2*, 496.
[8] P. Berini, *Adv. Opt. Photonics* **2009**, *1*, 484.
[9] A. N. Grigorenko, M. Polini, K. S. Novoselov, *Nat. Photonics* **2012**, *6*, 749.
[10] P. Tassin, T. Koschny, M. Kafesaki, C. M. Soukoulis, *Nat. Photonics* **2012**, *6*, 259.
[11] Z. Fei, A. S. Rodin, G. O. Andreev, W. Bao, A. S. McLeod, M. Wagner, L. M. Zhang, Z. Zhao, M. Thiemens, G. Dominguez, M. M. Fogler, A. H. Castro Neto, C. N. Lau, F. Keilmann, D. N. Basov, *Nature* **2012**, *487*, 82.
[12] J. N. Chen, M. Badioli, P. Alonso-González, S. Thongrattanasiri, F. Huth, J. Osmond, M. Spasenovi , A. Centeno, A. Pesquera, P. Godignon, A. Z. Elorza, N. Camara, F. J. García de Abajo, R. Hillenbrand, F. H. L. Koppens, *Nature* **2012**, *487*, 77.
[13] F. H. L. Koppens, D. E. Chang, F. J. García de Abajo, *Nano Lett.* **2011**, *11*, 3370.
[14] A. Principi, G. Vignale, M. Carrega, M. Polini, *Phys. Rev. B* **2013**, *88*, 195405.
[15] M. Gullans, D. E. Chang, F. H. L. Koppens, F. J. García de Abajo, M. D. Lukin, *Phys. Rev. Lett.* **2013**, *111*, 247401.
[16] J. D. Cox, F. J. García de Abajo, *Nat. Commun.* **2014**, *5*, 6725.
[17] Y. M. He, G. Clark, J. R. Schaibley, Y. He, M. C. Chen, Y. J. Wei, X. Ding, Q. Zhang, W. Yao, X. D. Xu, C. Y. Lu, J. W. Pan, *Nat. Nanotechnol.* **2015**, *10*, 497.
[18] V. W. Brar, M. S. Jang, M. Sherrott, J. J. Lopez, H. A. Atwater, *Nano Lett.* **2013**, *13*, 2541.
[19] H. G. Yan, X. S. Li, B. Chandra, G. Tulevski, Y. Q. Wu, M. Freitag, W. J. Zhu, P. Avouris, F. N. Xia, *Nat. Nanotechnol.* **2012**, *7*, 330.
[20] L. Ju, J. VelascoJr, E. Huang, S. Kahn, C. Nosiglia, H.-Z. Tsai, W. Yang, T. Taniguchi, K. Watanabe, Y. Zhang, G. Zhang, M. Crommie, A. Zettl, F. Wang, *Nat. Nanotechnol.* **2014**, *9*, 348.
[21] H. G. Yan, T. Low, W. J. Zhu, Y. Q. Wu, M. Freitag, X. S. Li, F. Guinea, P. Avouris, F. N. Xia, *Nat. Photonics* **2013**, *7*, 394.
[22] C. R. Dean, A. F. Young, I. Meric, C. Lee, L. Wang, S. Sorgenfrei, K. Watanabe, T. Taniguchi, P. Kim, K. L. Shepard, J. Hone, *Nat. Nanotechnol.* **2010**, *5*, 722.
[23] A. Woessner, M. B. Lundeberg, Y. D. Gao, A. Principi, P. Alonso-González, M. Carrega, K. Watanabe, T. Taniguchi, G. Vignale, M. Polini, J. Hone, R. Hillenbrand, F. H. L. Koppens, *Nat. Mater.* **2015**, *14*, 421.

© 2016 WILEY-VCH Verlag GmbH & Co. KGaA, Weinheim

15214095, 2016, 15, Downloaded from https://advanced.onlinelibrary.wiley.com/doi/10.1002/adma.201505765 by National Center For, Wiley Online Library on [15/10/2025]. See the Terms and Conditions (https://onlinelibrary.wiley.com/terms-and-conditions) on Wiley Online Library for rules of use; OA articles are governed by the applicable Creative Commons License

[24] V. W. Brar, M. S. Jang, M. Sherrott, S. Kim, J. J. Lopez, L. B. Kim, M. Choi, H. Atwater, *Nano Lett.* **2014**, *14*, 3876.
[25] A. Tomadin, F. Guinea, M. Polini, *Phys. Rev. B* **2014**, *90*, 161406.
[26] A. Principi, M. Carrega, M. B. Lundeberg, A. Woessner, F. H. L. Koppens, G. Vignale, M. Polini, *Phys. Rev. B* **2014**, *90*, 165408.
[27] S. Dai, Q. Ma, M. K. Liu, T. Andersen, Z. Fei, M. D. Goldflam, M. Wagner, K. Watanabe, T. Taniguchi, M. Thiemens, F. Keilmann, G. C. A. M. Janssen, S.-E. Zhu, P. Jarillo-Herrero, M. M. Fogler, D. N. Basov, *Nat. Nanotechnol.* **2015**, *10*, 682.
[28] P. N. Li, M. Lewin, A. V. Kretinin, J. D. Caldwell, K. S. Novoselov, T. Taniguchi, K. Watanabe, F. Gaussmann, T. Taubner, *Nat. Commun.* **2015**, *6*, 7507.
[29] S. Dai, Q. Ma, T. Andersen, A. S. Mcleod, Z. Fei, M. K. Liu, M. Wagner, K. Watanabe, T. Taniguchi, M. Thiemens, F. Keilmann, P. Jarillo-Herrero, M. M. Fogler, D. N. Basov, *Nat. Commun.* **2015**, *6*, 6963.
[30] E. Yoxall, M. Schnell, A. Y. Nikitin, O. Txoperena, A. Woessner, M. B. Lundeberg, F. Casanova, L. E. Hueso, F. H. L. Koppens, R. Hillenbrand, *Nat. Photonics* **2015**, *9*, 674.
[31] R. Fuchs, K. L. Kliewer, *Phys. Rev.* **1965**, *140*, A2076.
[32] M. Born, K. Huang, *Dynamical Theory of Crystal Lattices*, Clarendon Press, Oxford, England **1954**.
[33] S. Dai, Z. Fei, Q. Ma, A. S. Rodin, M. Wagner, A. S. McLeod, M. K. Liu, W. Gannett, W. Regan, K. Watanabe, T. Taniguchi, M. Thiemens, G. Dominguez, A. H. Castro Neto, A. Zettl, F. Keilmann, P. Jarillo-Herrero, M. M. Fogler, D. N. Basov, *Science* **2014**, *343*, 1125.
[34] J. D. Caldwell1, A. V. Kretinin, Y. G. Chen, V. Giannini, M. M. Fogler, Y. Francescato, C. T. Ellis, J. G. Tischler, C. R. Woods, A. J. Giles, M. H. Hong, K. Watanabe, T. Taniguchi, S. A. Maier, K. S. Novoselov, *Nat. Commun.* **2014**, *5*, 6221.
[35] L. Lindsay, D. A. Broido, *Phys. Rev. B* **2011**, *84*, 155421.
[36] Y. L. Li, H. G. Yan, D. B. Farmer, X. Meng, W. J. Zhu, R. M. Osgood, T. F. Heinz, P. Avouris, *Nano Lett.* **2014**, *14*, 1573.
[37] Z. Y. Fang, Y. M. Wang, A. E. Schlather, Z. Liu, P. M. Ajayan, F. J. García de Abajo, P. Nordlander, X. Zhu, N. J. Halas, *Nano Lett.* **2013**, *14*, 299.
[38] H. Buljan, M. Jablan, M. Soljacic, *Nat. Photonics* **2013**, *7*, 346.
[39] L. Wirtz, A. Rubio, R. A. de la Concha, A. Loiseau, *Phys. Rev. B* **2003**, *68*, 045425.
[40] E. H. Hwang, S. Das Sarma, *Phys. Rev. B* **2007**, *75*, 205418.
[41] T. Low, P. Avouris, *ACS Nano* **2014**, *8*, 16.
[42] E. H. Hwang, S. Das Sarma, *Phys. Rev. B* **1995**, *52*, R8668.
[43] E. H. Hwang, R. Sensarma, S. Das Sarma, *Phys. Rev. B* **2010**, *82*, 195406.
[44] M. Perner, P. Bost, U. Lemmer, G. von Plessen, J. Feldmann, U. Becker, M. Mennig, M. Schmitt, H. Schmidt, *Phys. Rev. Lett.* **1997**, *78*, 2192.
[45] U. Fano, *Phys. Rev.* **1961**, *124*, 1866.
[46] X. G. Xu, J. H. Jiang, L. Gilburd, R. G. Rensing, K. S. Burch, C. Y. Zhi, Y. Bando, D. Golberg, G. C. Walker, *ACS Nano* **2014**, *8*, 11305.
[47] J. A. Reissland, *The Physics of Phonons*, Wiley, Toronto **1972**.
[48] S. M. Xiao, V. P. Drachev, A. V. Kildishev, X. J. Ni, U. K. Chettiar, *Nature* **2010**, *466*, 735.
[49] J. Christensen, A. Manjavacas, S. Thongrattanasiri, F. H. L. Koppens, F. J. G. de Abajo, *ACS Nano* **2012**, *6*, 431.
[50] A. Vakil, N. Engheta, *Science* **2011**, *332*, 1291.
[51] X. S. Li, W. W. Cai, J. An, S. Kim, J. Nah, D. X. Yang, R. Piner, A. Velamakanni, I. Jung, E. Tutuc, S. K. Banerjee, L. Colombo, R. S. Ruoff, *Science* **2009**, *324*, 1312.

© 2016 WILEY-VCH Verlag GmbH & Co. KGaA, Weinheim

15214095, 2016, 15, Downloaded from https://advanced.onlinelibrary.wiley.com/doi/10.1002/adma.201505765 by National Center For, Wiley Online Library on [15/10/2025]. See the Terms and Conditions (https://onlinelibrary.wiley.com/terms-and-conditions) on Wiley Online Library for rules of use; OA articles are governed by the applicable Creative Commons License